Optical Measurements of Tsunami Inundation and Debris Movement in a Large-Scale Wave Basin

M. Rueben[1]; D. Cox[2]; R. Holman[3]; S. Shin[4]; and J. Stanley[5]

Abstract: This paper presents optical measurements of debris movement and tsunami inundation over an unobstructed beach in a laboratory wave basin. The debris consisted of rectangular boxes and was placed unconstrained on a flat section raised above the basin floor with no still water on the raised section. Debris movement was measured using two overhead video cameras and a novel object-tracking algorithm. Two standard optical techniques, wave edge detection and particle image velocimetry, were used to compare optical and in situ measurements of fluid velocity. The debris motion (position, velocity) in the onshore direction was found to be repeatable, but the offshore motion varied between trials because of the irregular nature of the flow field during the return. For debris in free translation, as the number of debris specimens increased, the peak average velocity decreased and the onset of the peak was delayed in the onshore direction. In the offshore direction, the velocity was lower by a factor 4–6 and was independent of the quantity of debris. The decrease in the peak onshore velocity with increasing amount of debris was observed for debris that undergoes an initial rotation. The peak onshore velocity was nearly independent of whether the initial motion was purely translational or a combination of rotation and translation. **DOI: 10.1061/(ASCE)WW.1943-5460.0000267.** © *2014 American Society of Civil Engineers.*

Author keywords: Tsunami; Laboratory experiments; Debris; Optical measurements; Argus camera; Inundation; Overland flow.

Introduction

Recent tsunami disasters around the world have caused devastating loss of life followed by difficult recovery processes. The tsunami that struck Tohoku, Japan on March 11, 2011, originated from a magnitude 9.0 earthquake off the Japanese coast and resulted in more than 15,000 deaths (Mori et al. 2011). Even tsunami barriers and RC buildings were destroyed in what was considered an area well prepared for a tsunami (Mori et al. 2011). Similar devastation was caused by other recent tsunamis, including the Sumatran tsunami in 2004 (Ruangrassamee et al. 2006; Saatcioglu et al. 2006), the Samoan tsunami in 2009 (Okal et al. 2010), and the Chilean tsunami in 2010 (Takahashi et al. 2010). Future tsunami events have the potential to cause similar damage. In the U.S. Pacific Northwest, the Cascadia subduction zone has an estimated 14% chance of causing a 9.0 magnitude earthquake in the next 50 years. This event would likely trigger a 10-m-high tsunami that would hit the coast in approximately 30 min (USGS Tsunami Pilot Study Working Group 2006). The size and speed of such a tsunami stresses the importance of studying tsunami-related hazards to reduce fatalities and damage.

Takahashi et al. (2010) conducted a field survey after the Chilean earthquake and tsunami and found that several hundred shipping containers in the southern district of Talcahuano Port had been moved shoreward and had caused secondary damage to coastal structures via tsunami-debris impact. Takahashi et al. (2010) reported that approximately 30% of the shipping containers from Talcahuano Port had drifted out to sea and that sunken objects, including ships, hindered navigation and delayed the resumption of port activities. In rare cases, video footage has provided a glimpse of this kind of large-scale debris motion. Naito et al. (2013) investigated the movement of fuel storage containers that were destroyed during the 2011 Tohoku tsunami, and Naito et al. (2014) developed a simple procedure to assess the potential for tsunami debris impact by studying satellite images taken after the 2011 event. Works by Foytong et al. (2013), Fritz et al. (2012), and Hayashi and Koshimura (2013), for example, have shown how the tsunami flow velocity can be estimated from video for the 2011 Tohoku tsunami. Arikawa and Yashizaki (2009), Arikawa et al. (2009), Matsutomi (2009), and Yeom et al. (2009) focused on debris impact and direct damage to structures. Although the tsunami-debris impact is an important issue, this paper focuses on the transport phase of debris motion, with no direct treatment of the impact itself.

It is noted that the work in this paper is part of a 3-year study related to tsunami inundation forces, and consists of two-dimensional hydraulic tests in a large-scale flume in Year 1 (e.g., Oshnack et al. 2009) followed by three-dimensional hydraulic tests in a large-scale basin in Year 2 (e.g., Park et al. 2013; Thomas and Cox 2012) as well as other work to develop design tools to resist tsunami forces (Park et al. 2012). Both experiments were conducted at the Network for Earthquake Engineering Simulation (NEES) Tsunami Facility located at Oregon State University (Corvallis, Oregon) and supported by the National Science Foundation (Washington, DC). The Year 1 and Year 2 experiments were, respectively, termed Housesmash and

[1]Graduate Student, College of Engineering, Oregon State Univ., Corvallis, OR 97331-6001. E-mail: ruebenm@onid.oregonstate.edu

[2]Professor, College of Engineering, Oregon State Univ., Corvallis, OR 97331-3212 (corresponding author). E-mail: dan.cox@oregonstate.edu

[3]Professor, College of Earth, Oceanic and Atmospheric Sciences, Oregon State Univ., Corvallis, OR 97331-5503. E-mail: holman@coas.oregonstate.edu

[4]Senior Researcher, Experimental Center for Coastal and Harbor Engineering, Chonnam National Univ., 50 Daehak-ro, Yeosu, Jeonnam 550-749, Korea. E-mail: sungwshin@gmail.com

[5]Senior Faculty Research Assistant, College of Earth, Oceanic and Atmospheric Sciences, Oregon State Univ., Corvallis, OR 97331-5503. E-mail: stanley@coas.oregonstate.edu

Note. This manuscript was submitted on October 28, 2013; approved on April 8, 2014; published online on May 29, 2014. Discussion period open until October 29, 2014; separate discussions must be submitted for individual papers. This paper is part of the ***Journal of Waterway, Port, Coastal, and Ocean Engineering***, © ASCE, ISSN 0733-950X/04014029(14)/$25.00.

Housesmash2 to distinguish them from other tsunami studies conducted at the facility. As part of the NEES program, the data were made available to other researchers at the conclusion of the project (e.g., Baldock et al. 2009). Therefore, the instrument naming convention and coordinate system from the facility are adopted in this paper for consistency.

This paper presents novel applications of optical techniques to observe and measure fluid and debris motion for certain trials within the Housesmash2 experiment and is a continuation of earlier work by Rueben et al. (2011) that developed optical methods for tsunami inundation measurements in laboratory basins. In addition to the development of optical measurement techniques, the aim of this work is to understand the characteristics of tsunami debris behavior under idealized conditions and to provide high-quality data that can be used as a benchmark for numerical simulation of tsunami debris motion. This paper is outlined as follows: "Facilities, Equipment, and Experiment" presents the large-scale, hydraulic model basin, instrumentation, and debris models; "Test Program" presents the trial procedures and rationale for the selection of initial debris configurations; "Bore and Surface Tracking" presents two optical techniques for quantifying wave motion—bore front tracking and free surface velocity estimation; "Debris Tracking Methodology" presents an optical technique for measuring the position and orientation of each debris specimen; "Repeatability of Debris Motion" discusses the repeatability of the debris motion for the configuration with four boxes and forced rotation; "Comparisons of Debris Position and Speed for Translation and Rotation" examines the effects of three aspects of the initial configurations on debris motion by comparing optical tracking results across different trials; and last section presents a "Summary and Conclusion," along with some recommendations for future research.

Facilities, Equipment, and Experiment

Wave Basin and Bathymetry

The Housesmash2 experiment (Thomas and Cox 2012) was conducted in the Tsunami Wave Basin (TWB) at the O. H. Hinsdale Wave Research Laboratory at Oregon State University. An overview photograph of the experimental setup is shown in Fig. 1 and a detailed schematic is shown in Fig. 2. The wavemaker specifications and wave basin bathymetry were identical to those used for a number of other studies at the same facility (Cox et al. 2008; Baldock et al. 2009; Rueben et al. 2011; Park et al. 2013; Thomas and Cox 2012). The description by Rueben et al. is adapted as follows for convenience:

- The basin was a rectangular box, 48.8 m long × 26.5 m wide × 2.1 m high; and
- The basin was equipped with a segmented, piston-type wavemaker with a maximum stroke of 2.1 m and maximum velocity of 2.0 m/s that was specifically designed to generate precise, long waves for tsunami research.

The coordinate system of the wave basin was defined as follows (see Fig. 2):

- X was positive in the direction of wave propagation (to the west) with $X = 0$ at the neutral position of the wavemaker;
- Y was positive to the south with $Y = 0$ along the centerline of the basin;
- Z was positive upward with $Z = 0$ on the basin floor;
- Beginning at the wavemaker, the bathymetry was comprised of a constant depth section for $0\ \text{m} < X < 10\ \text{m}$ at $Z = 0$ m followed by a 1:15 slope for $10\ \text{m} < X < 17.5$ m, followed by a 1:30 slope for $17.5\ \text{m} < X < 32.5$ m and ending with a raised flat section for $32.5\ \text{m} < X < 43.75$ m at elevation $Z = 1$ m above the basin floor (Fig. 2, elevation view); and

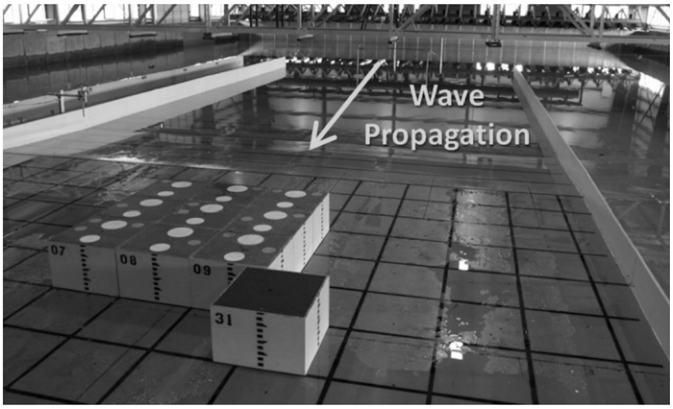

Fig. 1. Laboratory setup (Configuration 8): black gridlines form 60-cm squares and white plywood walls divide the NEES Housesmash2 tests from two other concurrent experiments; arrow indicates direction of wave propagation

- The impermeable bathymetry was constructed of smooth concrete with a float finish, and the roughness height was estimated to be 0.1–0.3 mm.

Starting at $X = 17.5$ m from the wavemaker, the basin was divided into three sections to allow for three experiments to take place concurrently (Fig. 2, plan view). This layout was identical to that described by Thomas and Cox (2012) and by Park et al. (2013), so their descriptions are adapted as follows for the reader's convenience:

- The Cannon Beach project occupied the southernmost 4.75-m width of the tank;
- The Texas A&M University (College Station, Texas) project occupied the northernmost 7.8-m width; and
- The Housesmash2 project was conducted in an 8.4-m-wide section in the center.

The Housesmash2 area was centered in the field of view of two high-resolution cameras that were part of the Argus observation network (Holman and Stanley 2007; Rueben et al. 2011).

- The projects were separated by smooth plywood walls anchored to the floor with metal brackets and sealed to eliminate the flow of water between the different projects;
- Two narrow channels existed between the study sections and were used for instrument amplifiers and to stage specimens for related studies;
- In the back (west) end of the basin, a thick layer of well-sorted crushed rock with nominal diameter of approximately 5 cm was used to dampen the reflected wave energy and to decrease the time needed to quiet the basin after each run;
- A rectilinear grid, composed of 3-cm-wide black lines with 0.6 × 0.6 m spacing, was painted onto the flat concrete section to accommodate the repeatable placement of the debris specimens; and
- The flat test section would correspond, approximately, to part of a shipping container yard at a port facility with a geometric scale of approximately 1:20.

Instrumentation

The in situ data for this project were recorded and stored using a 64-channel PXI-based real-time data acquisition system (National Instruments, Austin, Texas) with a sampling rate of 50 Hz and duration of approximately 80 s. The sampling rate was set at the maximum allowable rate for the acoustic-Doppler velocimeters (ADVs, Nortek Vectrino, Rud, Norway). The sampling duration was sufficient to capture the full inundation as well as much of the return

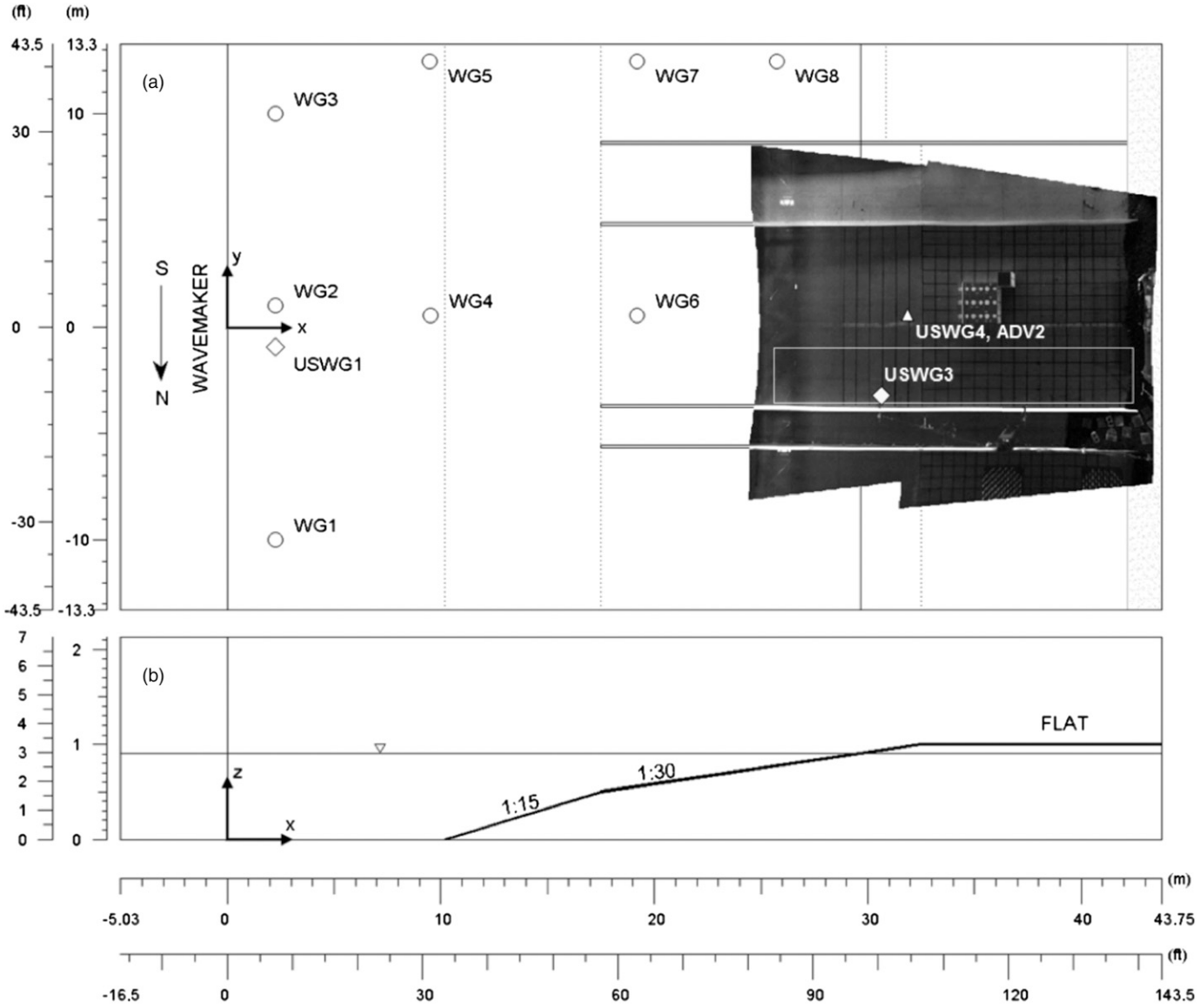

Fig. 2. Schematic of the TWB instrumented for Kinematics Trial 15: (a) plan view includes locations of wire resistance wave gauges (open circles); ultrasonic wave gauges (open diamonds); a USWG-ADV pair (open triangle); merged view from both overhead Argus cameras is shown on the plan view; (b) elevation view shows uniform bathymetry along shore and mean water level

flow, although the in situ velocity in the leading edge of the tsunami could not be measured by ADVs from air entrainment. All time values in this paper reference the data acquisition system and camera images were synchronized to these values in postprocessing.

Fig. 2 shows the location of the in situ instrumentation used for this study. Eight wire resistance wave gauges (WGs) manufactured in-house and six ultrasonic wave gauges (USWGs) (Model No. TS-30S1-IV, Senix, Bristol, Vermont), were mounted in the basin. Of these, two ultrasonic wave gauges (USWG3 and USWG4) were located onshore for the SlidingBox trials. For this work, these two gauges were primarily used for synchronizing the camera data with the in situ data. For the Kinematics Trials, the USWG4 was colocated with an acoustic-Doppler velocimeter (ADV2) near the centerline of the basin at $X = 31.89$ m, $Y = 0.54$ m.

Optical instrumentation for this work was identical to that used by Rueben et al. (2011). Two Argus cameras (Redford Charter Township, Michigan) were located directly over the basin at tank coordinates $X = 39.98$ m, $Y = -0.96$ m, and $X = 32.41$ m, $Y = 10.78$ m. The Argus cameras were Scorpion FireWire imager models featuring $1{,}280 \times 960$-pixel, 8-bit, Bayer-encoded charge-coupled device sensor chips and 4.5-mm lenses spanning a 69° horizontal field of view. The spatial resolution and long-term stability of these same cameras were reported by Rueben et al. (2011). Frame rate was set to 5 Hz for Kinematics trials and 2 Hz for SlidingBox trials. Each pair of collected frames from the two cameras was synchronized and projected to a rectified plan view at a single elevation (Z-value), and then merged into a single image (e.g., Rueben et al. 2011). Rectifying and merging camera frames was automated by tools included in the Argus Database as used by Rueben et al. (2011) and described by Holman and Stanley (2007). An example pair of images merged to $Z = 1$ m is shown in Fig. 2 to depict the overall field of view.

Debris Specimens for Optical Tracking

The debris specimens were constructed from 12.7-mm (0.5-in.) thick plywood. Each box had a nominal footprint of 60×60 cm and was nominally 40 cm tall. The sides of each box were painted blue with a black number on one side for unique identification from a distance

and a black scale to facilitate run-up observations via webcam. Nominal dry weights were 14.5 kg (±1 kg) per box. The coefficient of friction between the wet plywood debris and smooth concrete floor of the basin was not measured and is estimated from the literature to be in the range of 0.2 to 0.3 (Gorst et al. 2003). From the symmetry of the box construction, the center of gravity of the debris is located in the center in the box ($x = y = 30$ cm, $z = 20$ cm) and the draft was 4.0 cm (±0.3 cm). Although debris in an actual tsunami can be of irregular shape (for example, cars, ships, partially destroyed wooden buildings) as was mentioned by one of the reviewers, the idealized shape of a rectangular box was chosen for simplicity. Given that the tsunami bore-height was nominally 15 cm for this experiment, it would suggest a length scale of approximately 1:20 for large tsunami inundation. Therefore, the characteristic debris length of 0.60 m in the experiment would correspond to 12 m in prototype or approximately the length of a standard shipping container (12.19 m).

One box, designated with a black lid, was loaded with concrete blocks and remained stationary throughout each trial to act as an obstacle for other debris. This box will be referred to as the *stationary box* for the remainder of this paper. The remaining boxes were empty and did not fill with water during the tests. They were allowed to slide or float with each wave and are termed *sliding boxes*. The lids of the sliding boxes were painted to facilitate video image tracking: two yellow circles (15 and 20 cm in diameter) for tracking orientation and up to six orange circles (10 cm in diameter) for identifying the box number from above, all on a blue background for contrast. Unique box numbers were used to demonstrate a method for tracking individual boxes. All paints were low-gloss to prevent reflections of the ceiling lights from reducing the contrast between colors in the images. Fig. 1 shows an example configuration of boxes (Configuration 8) on the shore section of the TWB floor. The direction of wave propagation is indicated by an arrow for reference, and this was also the positive X-direction in the TWB coordinate system (see Fig. 2).

Test Program

Experimental Process

The experimental procedure was similar to that used for previous Housesmash2 trials, so this section includes descriptions adapted from Thomas and Cox (2012) for convenience. The experiment was conducted with a water depth of 90.56 cm with a SD of 0.13 cm based on measurements before each trial. With this water level, the still-water shore line was located at $X = 29.8$ m and approximately 3 m from the start of the flat inundation section at $X = -3.0$ m (see Fig. 2). All of the waves broke seaward of this position and advanced over the flat section as a broken bore. An error function was used to generate the paddle displacement so that the full 2-m stroke of the wavemaker could be used, even for relatively small tsunami heights of 10 cm or less, thereby maximizing the duration of the inundation process. Conventional solitary wave-generation techniques (e.g., Goring 1978) would have limited the inundation for the smaller wave heights. Only one wave type, denoted erf = 7 s, was generated for the specific trials chosen for this paper. For this wave type, the wavemaker paddles were actuated according to an error function with a 7-s period and 2-m displacement. Fig. 3 shows an example of in situ data from Kinematics Trial 15. Fig. 3(a) shows the wavemaker displacement time series and transient wave of approximately 10-cm amplitude. The free surface time series is fairly symmetrical leaving the waveboard [Fig. 3(a)] and continues to have a fairly symmetrical shape and constant amplitude as it propagates over the flat section of the basin [Fig. 3(b)] for 20 s $< t <$ 30 s. The free surface becomes asymmetric and increases in height as the wave propagates over the slope [Fig. 3(b), WG6], breaks, and propagates over the flat, raised portion of the basin as a broken bore [Fig. 3(c)]. The bore velocity [Fig. 3(d)] is highest at the leading edge, and the ADVs had difficulty capturing the velocity in the leading edge from air entrainment.

The entire run sequence—wave generation, propagation, and inundation—had a duration of approximately 2 min. Subsequently, data were uploaded to a local data repository and all data channels were inspected visually before the start of the next run. Any remaining water was removed from the flat section of the beach using squeegees, specimens were positioned according to the next configuration, and the basin was allowed to calm before the start of the next trial.

Debris Specimen Configurations

Each of the SlidingBox trials began with the debris specimens arranged in a predetermined initial configuration (e.g., Configuration 5). After wave generation, the bore propagated over the raised section and moved the boxes onshore. The stationary box, when used, remained as a fixed obstacle, and its purpose was to force the other boxes to be rotated. Fig. 4 shows the seven unique configurations chosen for this study. Each configuration was tested only once because of time constraints except Configuration 4, which was used for six trials to verify repeatability.

The seven configurations were designed such that three aspects of initial debris configurations could be studied: the number of boxes, the induced rotation, and the segmentation of groups. For Configurations 1, 3, and 7 (first column of Fig. 4), the box motion was

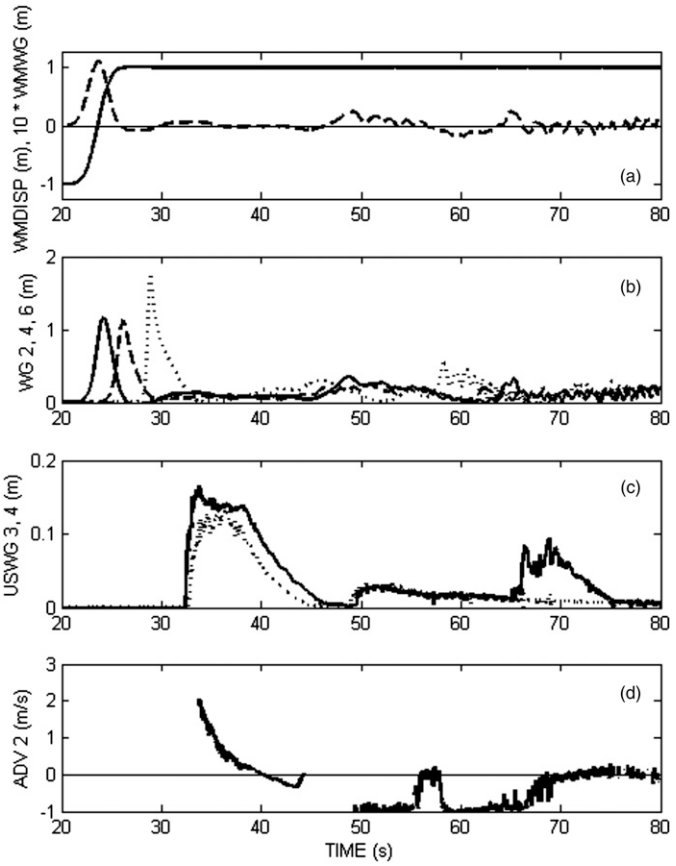

Fig. 3. Example wavemaker and in situ time series data from Kinematics Trial 15: (a) wavemaker displacement (solid line) and 10× wave height at wavemaker paddle (dashed line); (b) wave height at WG2 (solid line); WG4 (dashed line); WG6 (dotted line); (c) bore height at USWG3 (solid line); USWG4 (dotted line); (d) cross-shore fluid velocity at ADV2

J. Waterway, Port, Coastal, Ocean Eng., 2015, 141(1): 04014029

primarily translation with little rotation. The number of boxes was increased from 1 to 4 to 9, respectively, while maintaining a square pattern. For Configurations 2, 4, and 8 (second column of Fig. 4), the setup was identical to Configurations 1, 3, and 7, except that a fixed box was added to induce rotation. Configuration 12 (third column of Fig. 4) was added with four boxes joined together to compare the motion with the four individual boxes in Configuration 4.

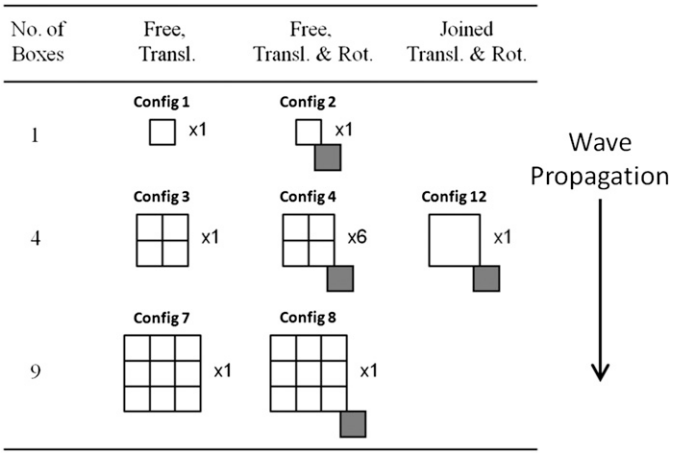

Fig. 4. Schematic diagrams of the box configurations; white boxes are free to move along the floor and gray stationary box is fixed; number of repetitions is given, e.g., $\times 6$ indicates six repetitions of the same configuration

Bore and Surface Tracking

The bore motion over the raised section was studied prior to introducing the box specimens described in the previous section. Bore motion was analyzed using two optical techniques on five Kinematics trials with wave type erf $= 7$ s. Video frames were projected to shore level ($Z = 1$ m) when measuring wave motion. The bore edge position was calculated on a frame-by-frame basis using an algorithm similar to that described by Rueben et al. (2011). Useful corollaries of the bore edge position include the time of debris contact and the average bore velocity at a desired time or location. In addition, the free surface velocity of the inundation was estimated by tracking the movement of surface foam. This analysis was carried out using the *MATLAB R2011b* Particle Image Velocimetry (MPIV) toolbox, which tracks the motion of persistent shapes across successive video frames. Use of MPIV was limited to the specific times and locations in which high-contrast foam was visible.

Fig. 5 shows the average results of both the edge tracking and the surface velocities for five frames, each 1.0 s apart, during the initial inundation for Kinematics Trials 15, 28, 32, 37, and 42. The leading edge is shown as a dashed line with ± 1 SD calculated from the edge detection algorithm, and the surface velocities are shown as velocity vectors, with the vector scale of 3 m/s shown near

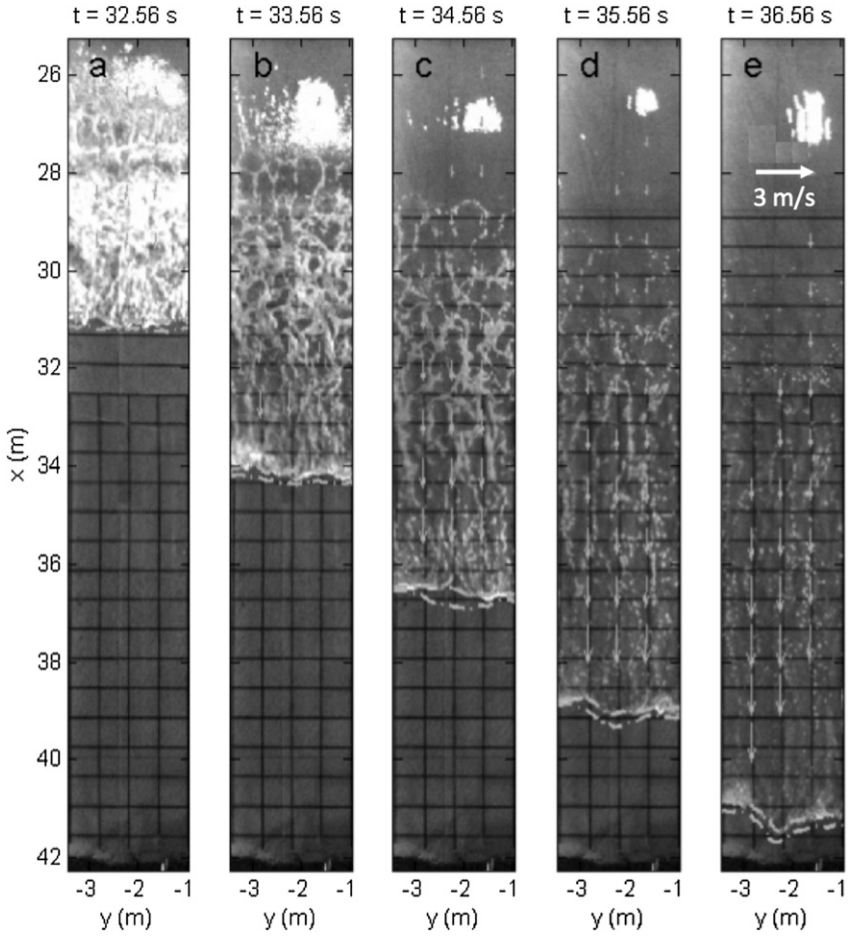

Fig. 5. Bore and surface tracking results from Kinematics Trials 15, 28, 32, 37, and 42 shown over merged images from Kinematics Trial 28; wave type for these trials is erf $= 7$ s; arrows indicate surface velocity estimations from MPIV analysis; dashed lines show ± 1 SD from mean wave-edge position as calculated by edge detection analysis

the top of Fig. 5(e). Fig. 5(a) shows the broken bore at $X = 31$ m just prior to the inundation over the raised section starting at $X = 32.5$ m. Figs. 4(b–d) show the inundation past the initial starting position of the debris to be placed at $X = 34.5$ and that the velocity is uniform across the basin width in the absence of debris. Fig. 5(e) shows the inundation well past the initial debris positions. Here, the leading bore edge becomes less uniform across the basin width, and the loss of persistent foam decreases the number of velocity vectors resolved by the MPIV.

Fig. 6 shows how the optical and in situ measurements were combined to compensate for the inability of the ADVs to capture the leading part of the flow because of air entrainment and the inability of the optical method to capture the surface velocity later in the flow because of a lack of persistent foam. The measurements were taken for Kinematics Trial 15 with in situ measurements taken from colocated USWG4 and ADV2 at $X = 31.89$ m, $Y = 0.54$ m. Fig. 6(a) shows the free surface of the bore in the range $32\ \text{s} < T < 38$ s and that the signal is well resolved by the USWG despite the presence of air entrainment. The leading edge arrives at $T = 32.8$ s and reaches a maximum approximately 3 s later. Fig. 6(b) shows the combined in situ and optical velocity measurements over the same time. The in situ velocity (dots) can be resolved after the leading part of the flow has passed ($T > 33.6$ s), but completely misses the leading-edge velocity ($32.8\ \text{s} < T < 33.6$ s). The vertical lines show the optical measurements of the surface velocity using the MPIV routine. They agree well with the in situ measurements and provide velocity information sooner than the ADV does, but not at the leading edge. The velocity can be resolved at the leading edge by the edge-tracking routine and is shown by the star symbol. Combining these three velocimetry techniques allows for a line of best fit [Fig. 6(b), solid line] that represents a reasonable estimation of the fluid velocity for the entire time period of interest. Fig. 6(c) shows the momentum flux estimated as the product of the free surface times the square of the velocity. Although the momentum flux is not used elsewhere in this paper, it may be a useful quantity for predicting the initiation of debris movement or damage to coastal structures. Fig. 6(c) shows that the peak momentum flux occurs approximately 0.3 s after bore arrival and 2.7 s before the maximum height.

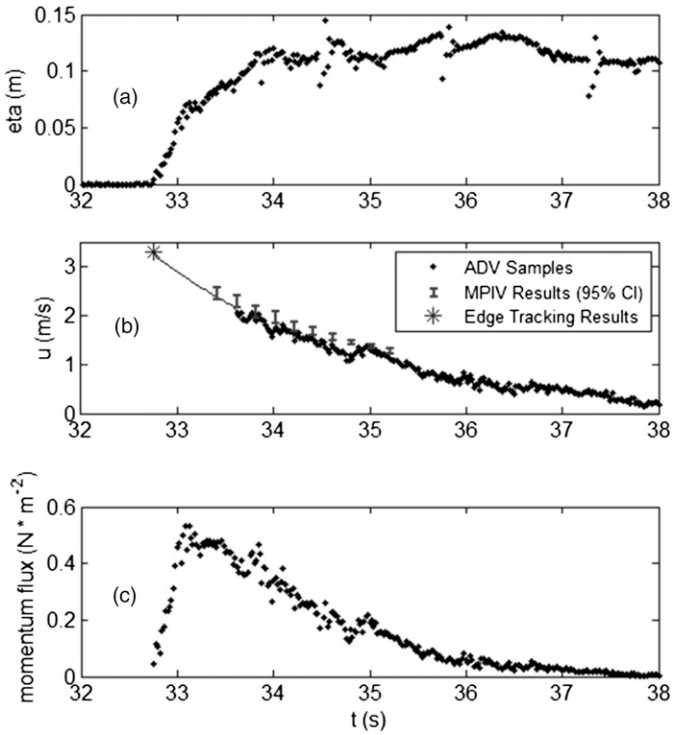

Fig. 6. Combined in situ and optical data for Kinematics Trial 15 at $X = 31.89$ m, $Y = 0.54$ m for erf = 7 s wave: (a) wave height as measured by USWG4; (b) fluid velocity measurements from leading-edge tracking (star); MPIV analysis (error bars, 95% confidence interval); ADV2 (dots); best-fit line used to calculate momentum flux; (c) momentum flux

Debris Tracking Methodology

An image processing technique was developed for measuring the position and orientation of multiple debris specimens using a unique color scheme for the box lids. Video frames were projected to box lid level ($Z = 1.4$ m) when measuring box motion. The hue/saturation/value color map was used to analyze the images instead of the more familiar red/green/blue system. Hue is a pixel's color, saturation is the amount of color, and value is the brightness of that color. The yellow, orange, and blue colors for the box lids were chosen such that they could be differentiated in all three channels, thereby increasing object-tracking certainty.

Fig. 7 shows an example of the box-tracking process. Fig. 7(a) shows the original image. The first step in the box-tracking algorithm is to identify the background on the box lid using handpicked thresholds [Fig. 7(b)]. The outline of the background is used as a mask to isolate the box lid for further processing by eliminating the rest of the image. The two middle dots are identified next within the isolated box lid image [Fig. 7(c)]. By counting the pixels in each dot, the algorithm can distinguish between the two different dot sizes and check to make sure each dot is of the expected size (i.e., that the entire circle has been selected). The middle dots define the box position and orientation within the Tsunami Wave Basin's local coordinate system. These data are then used to infer the expected locations of the six dots on the side that indicate the box number. Checking for each dot on the side at its expected location yields the box number via a binary numbering system used for this experiment. This completes the box-tracking algorithm, inasmuch as all four aspects of the box state have now been determined: box number, X-position, Y-position, and orientation angle [Fig. 7(d)].

Fig. 8 shows an example of the video frames overlaid with tracking results for Configuration 2. Fig. 9 summarizes the initial debris motion in configurations with rotation induced by a stationary box for a single box [Configuration 2, Figs. 8(a and b)] and for a single large box composed of four boxes joined together [Configuration 12, Figs. 8(c and d)], four individual boxes [Configuration 4, Figs. 8(e and f)], and nine individual boxes [Configuration 8, Figs. 8(g and h)]. Figs. 8(a, b, e, and g) show the initiation of the box motion with large impact, and Figs. 8(b, d, f, and h) show the subsequent rotation of the debris and wave reflection. Note the dissimilar nature of the joined four boxes [Fig. 8(d)] and free four boxes [Fig. 8(f)], and that multiple free boxes form columns [Figs. 8(f and h)] in the direction of flow. For the case of nine free boxes with no rotation (Configuration 7), the columns of debris persisted until the stall point, and the axis of the column was oriented perpendicular to the reflected waves (figure not shown for brevity).

Repeatability of Debris Motion

The configuration with four free boxes and forced rotation (Configuration 4) was repeated for six trials to estimate the repeatability for this and other configurations and is summarized in Figs. 9–12. Fig. 10(a) shows the position of centroid of Box 2 for

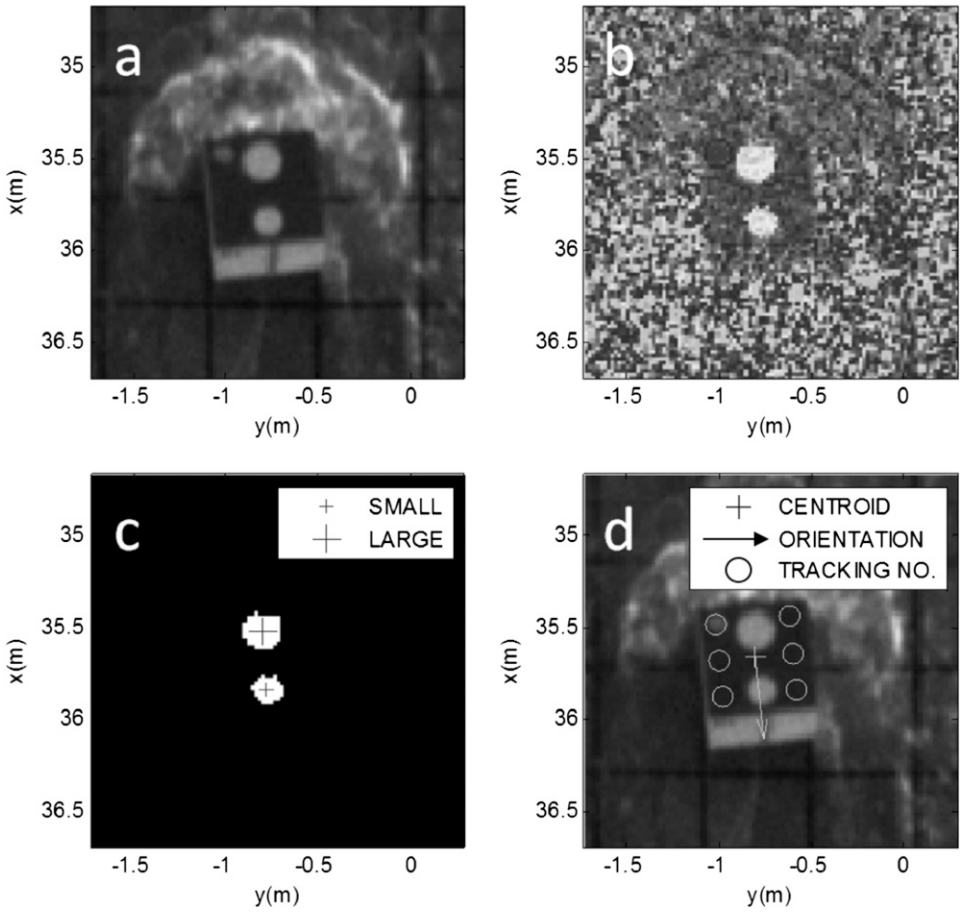

Fig. 7. Box-tracking process: (a) original image rectified to box-lid height; (b) hue channel isolated using hue/saturation/value color map; (c) dots located and identified by size; (d) tracking results plotted over original image

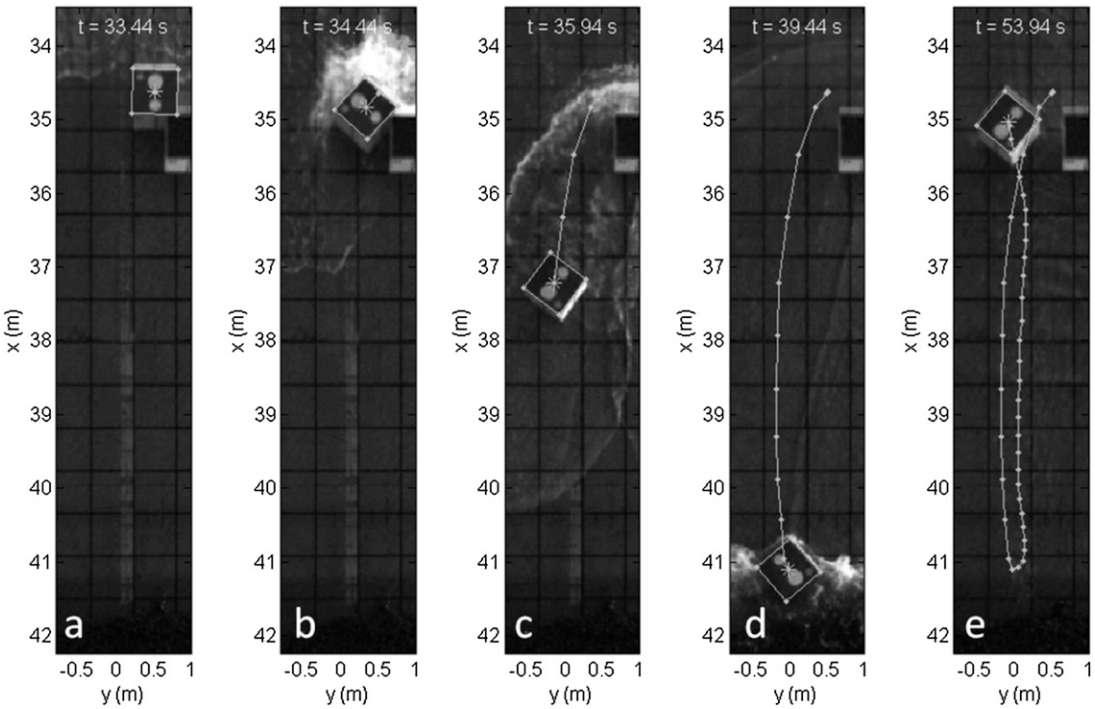

Fig. 8. Cropped, merged images from Trial 31, boxes arranged in Configuration 2: (a–e) each image is from a specific frame with time indicated at top of image; box-tracking algorithm is demonstrated by box outline and box center position (star); box velocity can be inferred from dot spacing; frame rate is 2 Hz

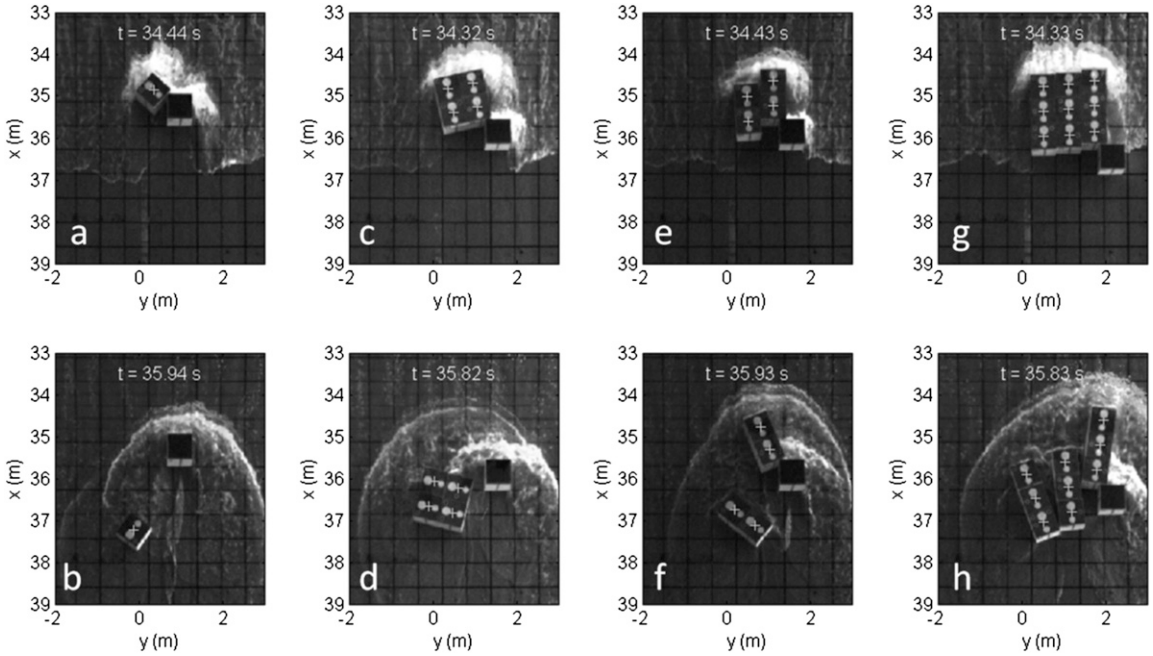

Fig. 9. Comparison of cropped, merged images at similar times across four trials: (a and b) Trial 31, Configuration 2; (c and d) Trial 65, Configuration 12; (e and f) Trial 33, Configuration 4; (g and h) Trial 37, Configuration 8; (a–h) each image is from a specific frame with time indicated at top of image; box-tracking algorithm is demonstrated by box centers (crosses)

each of the six trials, and Fig. 10(b) shows the average of the onshore motion plus the SD. The repeated motion of the other four boxes was similar in that the onshore motion was predictable until the stall point, but the offshore motion such as the path and final stop points varied. Fig. 11(a) shows the combined centroid position computed for the four free boxes for each of the six trials, and Fig. 11(b) shows the average centroid position with the SD of in the Y-direction for the onshore motion. Similar to Fig. 10, Fig. 11 shows that for the same configuration the onshore motion was highly repeatable, whereas the offshore motion had divergent paths. Figs. 12(a and b), shows the stall points and final stopping points, respectively, for each of the four boxes for the six runs. It is interesting to note that the stall points (most landward position) are highly clustered for all six runs [Fig. 11(a)], whereas the final stopping points have large variability [Fig. 11(b)]. Somewhat surprisingly, some of the boxes came to rest very close to their initial starting points for several of the runs. In no cases did the boxes drift out to sea (that is, all boxes remained on the flat section of the basin and landward of the still-water shoreline for this condition).

Fig. 13 shows the X-directed velocity (in the direction of wave propagation) for the four boxes for each of the six trials. Similar to Figs. 10 and 11, it can be observed that the onshore motion (positive velocity) was highly repeatable and that the offshore velocity (negative velocity) was more variable. The experimental setup and wavemaker were carefully controlled for these tests, leading to repeatable results for the onshore motion. It is speculated that the variability in the offshore position may be based on several factors, for example, the temporary grounding of boxes that can clearly be seen in Fig. 13 for Box 3 at $t = 45$ s for some of the trials, but not others. Temporary grounding was not observed in the three other boxes in Fig. 13, so other phenomena must be responsible. It is speculated that the boxes may have been subjected to interactions with persistent eddies produced by the fixed box or by the free boxes or both during the return flow.

Comparisons of Debris Position and Speed for Translation and Rotation

This section presents four systematic comparisons among the debris configuration, as follows:

1. Increasing amount of debris in free translation;
2. Increasing amount of debris in forced rotation;
3. Single debris in free translation and forced rotation; and
4. Four free boxes in translation and forced rotation with four boxes joined.

Note that when multiple boxes are used, only the centroid of all the boxes is shown, similar to Fig. 10(b).

Fig. 14 compares debris in free translation with increasing number of debris specimens: one, four, and nine boxes for Configurations 1, 3, and 7 as shown in Fig. 4. Fig. 14(a) shows the X-Y position of the average centroid and indicates that the motion of the debris centroid is qualitatively similar for each case. The onshore motion is essentially one-dimensional during the onshore motion, and after the stall point during the return motion, there is a preference for the debris to move in the negative Y-direction, probably owing to irregularities in the concrete floor. The location of the stall point moves seaward and the amount of debris increases. Fig. 14(b) shows the corresponding X-directed velocity (u is positive onshore) for each configuration. Fig. 14(b) shows that as the number of debris pieces decrease, the centroid reaches a higher peak velocity and the peak occurs sooner, indicating that the close proximity of the debris alters the local flow field. In contrast, during the return flow, the centroids reach the same velocity (approximately 0.25 m/s seaward) regardless of the amount of debris, presumably because the debris are dispersed and do not alter the local flow field. This is consistent with observations that the debris remained in columns during onshore flow when multiple boxes were tested and that these columns broke apart when the flow reversed. Fig. 14(b) shows that the average centroid motion stops at approximately the same time ($t = 56$ s) regardless of the amount of debris [Fig. 14(b)], although

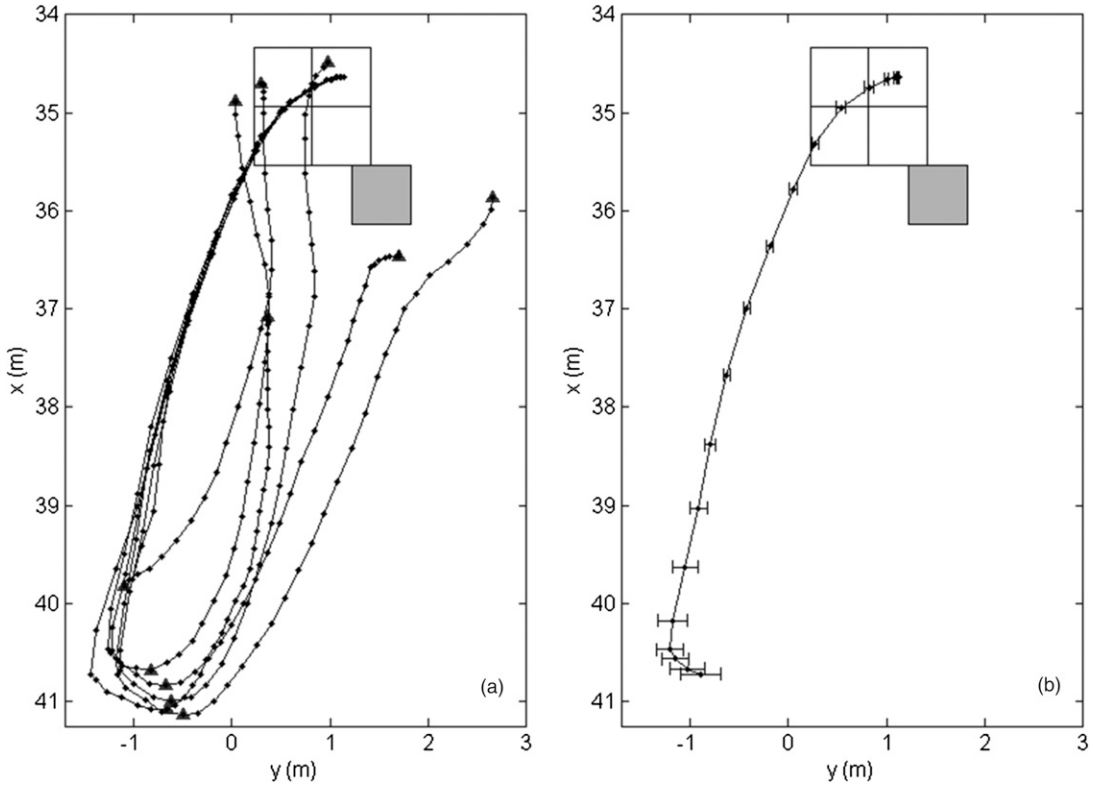

Fig. 10. Repeatability of Box 2 path for Configuration 4 over six trials (Trials 33, 39–43); for each trial: (a) Box 2 center positions (dots); stall points where X-velocity reverses (closed triangles); stop points where the box settles (closed triangles); (b) mean Box 2 path across all six trials for the onshore ($+X$-direction) motion only; error bars show standard error of Y-position at each time step with 95% confidence interval; schematic of initial box positions from Fig. 4 shown for Configuration 4 in both plots for reference and scale

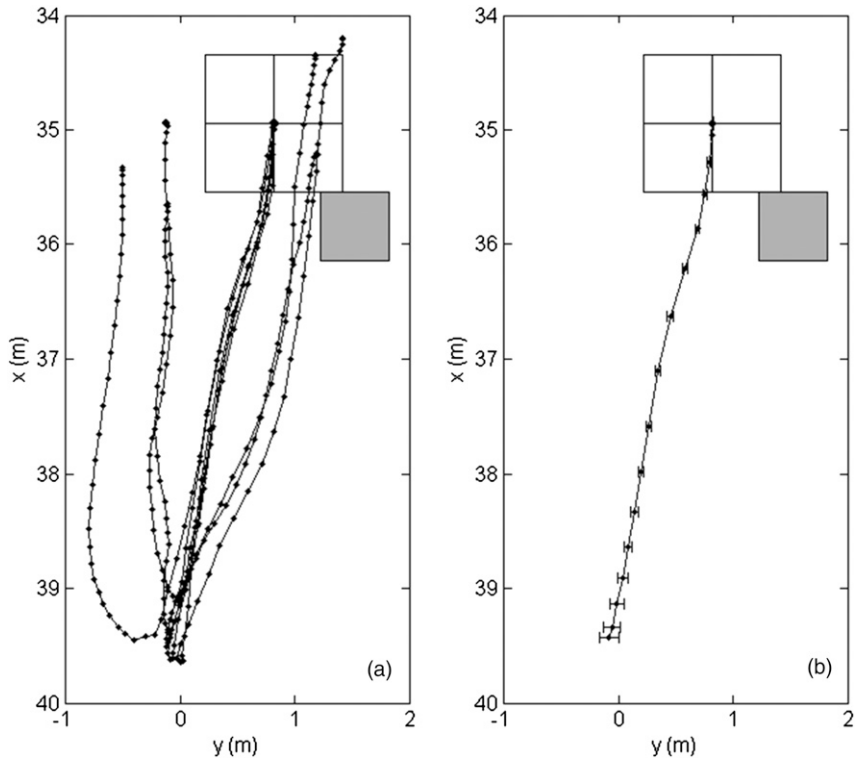

Fig. 11. Repeatability of centroid path for Configuration 4 over six trials (Trials 33, 39–43): for each trial, (a) box centroid positions (dots); the centroid is the arithmetic mean of all box centers for a single time step; (b) mean centroid path across all six trials for the onshore ($+X$-direction) motion only; error bars show standard error of Y-position at each time step with 95% confidence interval

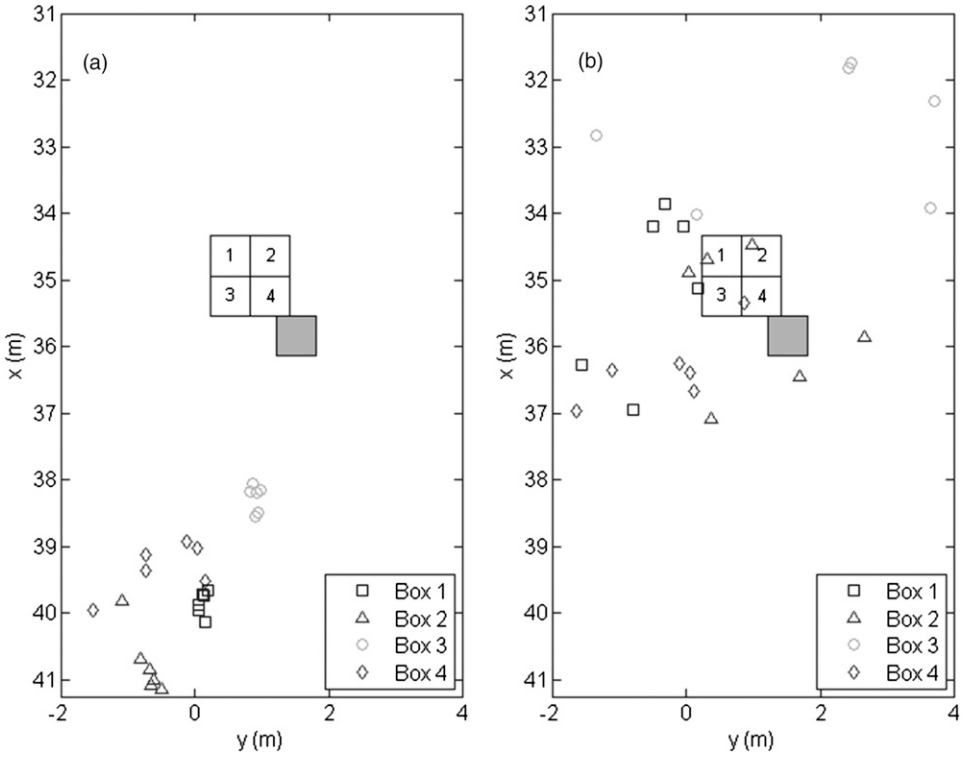

Fig. 12. Repeatability of Configuration 4 expressed via stall points and stop points for each box over six trials (Trials 33, 39–43): (a) stall points, the positions where cross-shore (X) velocity reverses from onshore ($+X$) to offshore ($-X$) based on the reflected wave; (b) stop points, the final positions of each box at the end of the trial; box numbers in schematic correspond to symbols specified in legend

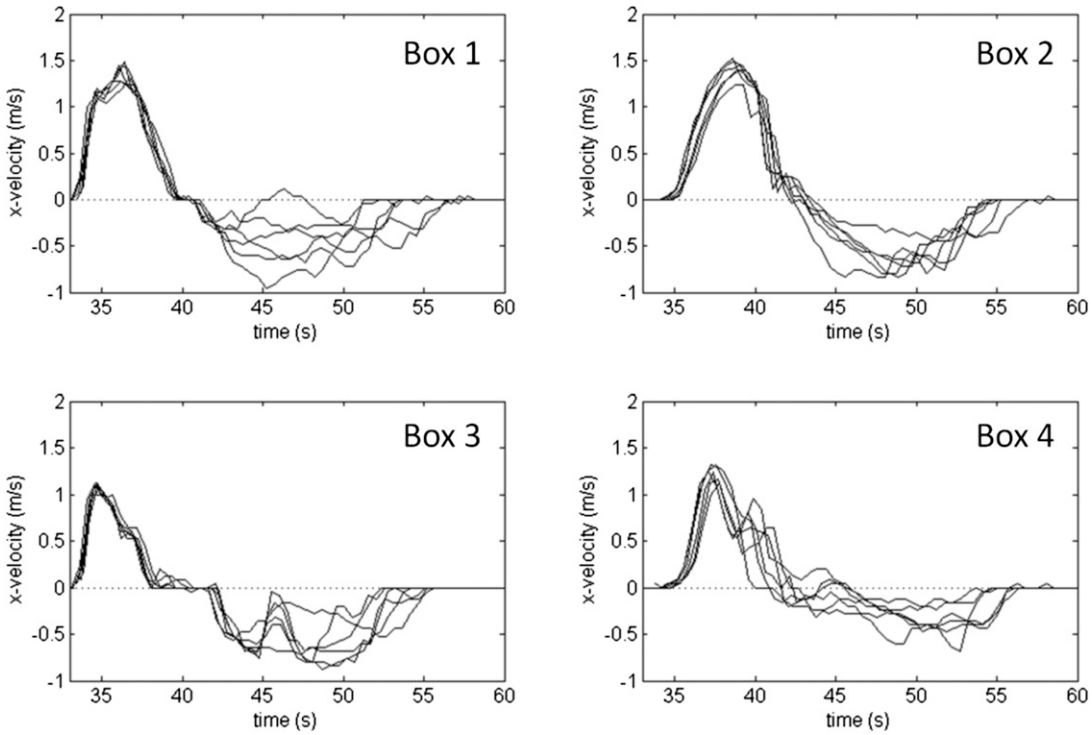

Fig. 13. Velocity repeatability for six trials (Trial 33, 39–43) conducted with Configuration 4; each plot shows cross-shore (X) velocity for a single box coplotted over time for all six trials

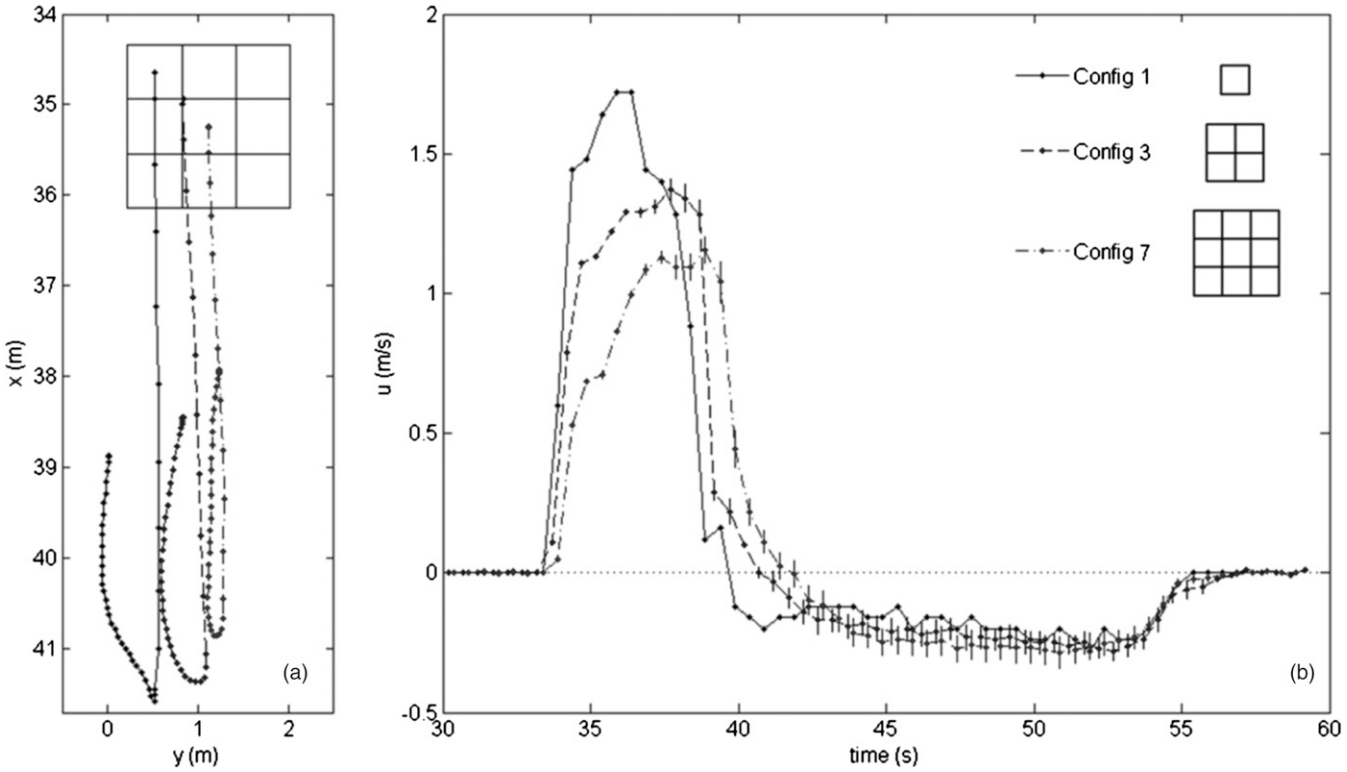

Fig. 14. Configurations 1, 3, and 7: (a) path positions and (b) cross-shore (X-direction) velocities for multibox configurations (Configurations 3 and 7) are for the centroid, which is the arithmetic mean of all box centers for a single time step; error bars for multibox configurations represent standard error of box velocities with 95% confidence intervals; schematic of initial box positions from Fig. 4 shown for Configuration 7 in plot (a) for reference and scale

the final stopping point of the average centroid is slightly different [Fig. 14(a)].

Fig. 15 compares debris in forced rotation with increasing number of debris specimens: 1, 4, and 9 for Configurations 2, 4, and 8 as shown in Fig. 4. Similar to Fig. 14, Fig. 15(b) shows the average centroid position, and Fig. 15(c) shows the corresponding velocity. It is noted that the line in Fig. 15(a) for Configuration 2 corresponds to the line shown in Fig. 8(e). In contrast to Fig. 14, there are obvious qualitative differences among the three cases in forced rotation. The average centroid positions, for example, shown in Fig. 15(b), are qualitatively different: during return flow, the centroid moves in the negative Y-direction for Configurations 2 and 4 and in the positive Y-direction for Configuration 8. The velocity time series also no longer have a systematic variation with increasing number of boxes. The peak velocities for Configurations 4 and 8, for example, reach nearly the same peak velocity and at the same time. Moreover, there is significant variation of the position of the individual boxes (as indicated by the size of the error bars) during the onshore flow. This is because several of the boxes were hung up on the stationary box as can be seen in Fig. 9(f) for Configuration 4, and 8 h for Configuration 8. During the return flow, there is significant difference in the offshore velocities of the centroids, ranging from approximately -0.6 m/s for the single box to -0.25 m/s for the nine boxes. Moreover, the final stopping time is different, ranging from $t = 54$ s to $t = 57$ s. Interestingly, however, the centroids come to rest at nearly the same place where they started in the range of 35 m $< x <$ 36 m.

Fig. 16 compares free translation (Configuration 1) and forced rotation (Configuration 2) for a single box and compares forced rotation for the single box (Configuration 2) and a single box formed by joining four boxes together (Configuration 12). It is noted that the motion of Configurations 2 and 12 can be seen qualitatively in Figs. 9(a and b) and 9(c and d), respectively. Fig. 16 shows that the translation and rotation cases for a single box have different onshore trajectories as expected and that the boxes reach nearly the same peak onshore velocity at nearly the same time. Their offshore-directed motions, however, are quite different, with the translating box moving slower by a factor of 2. The translating box reaches a final stopping point midway between the initial point and the stall point, whereas the rotating box comes to rest at approximately the same place that it started. In comparing the two rotating boxes of different sizes, one can see a pattern reminiscent of Fig. 14 in that the onshore peak velocity is smaller and happens later as the size of the debris area increases. During the return flow, the offshore-directed velocities are approximately the same for the small and the large boxes, similar again to what was observed for the return flow for Fig. 14.

Finally, Fig. 17 compares debris with the same area (four boxes) for free translation (Configuration 3), forced rotation of four individual boxes (Configuration 4), and forced rotation of four combined boxes (Configuration 12). In comparing Configurations 3 and 12, it appears that centroid trajectories are different but the peak velocities are somewhat similar in magnitude and time of occurrence. During the offshore motion, the final resting position of the average centroid of the translating boxes is between the stall point and initial starting point. For Configuration 12, the final resting point is near the initial starting point. Moreover, the offshore velocity of Configuration 12 is approximately twice as large as the average centroid velocity in Configuration 3.

These findings are entirely consistent with the observations for the single boxes in translation (Configuration 1) and rotation (Configuration 2). On the other hand, in comparing the velocities of

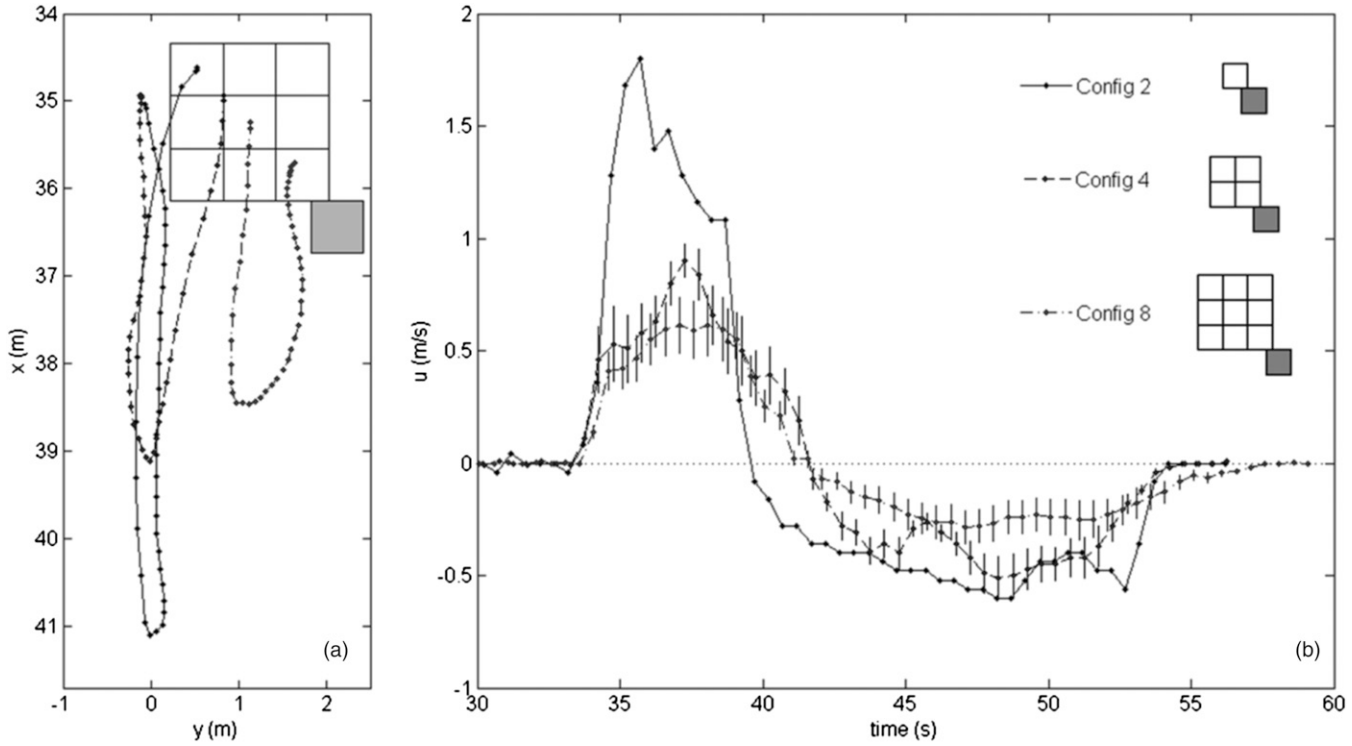

Fig. 15. Configurations 2, 4, and 8: (a) path positions and (b) cross-shore (X-direction) velocities for Configurations 4 and 8 are for the centroid of all sliding boxes; schematic of initial box positions from Fig. 4 shown for Configuration 8 in plot (a) for reference and scale

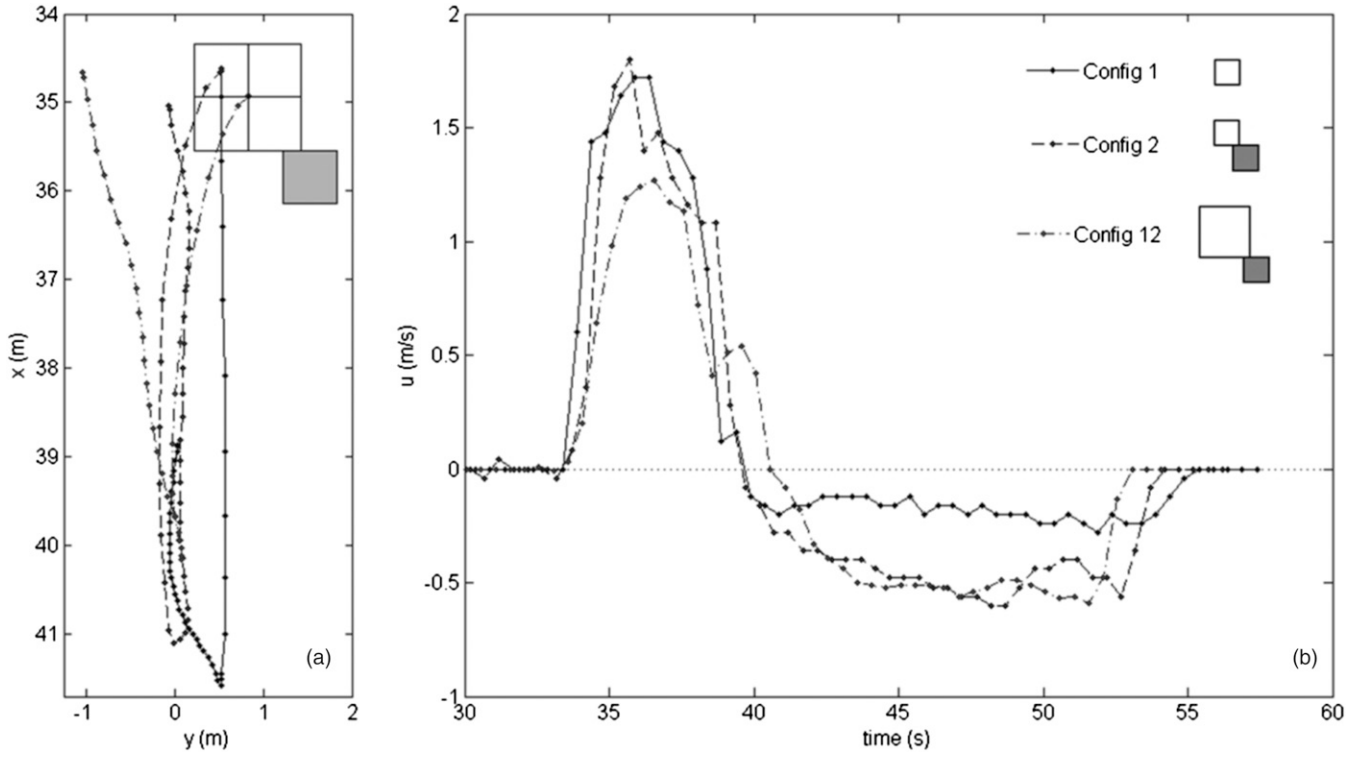

Fig. 16. Configurations 1, 2, and 12: (a) path positions and (b) cross-shore (X-direction) velocities for Configuration 12 are for the centroid of the four-box square; schematic of initial box positions from Fig. 4 shown for Configuration 12 in plot (a) for reference and scale

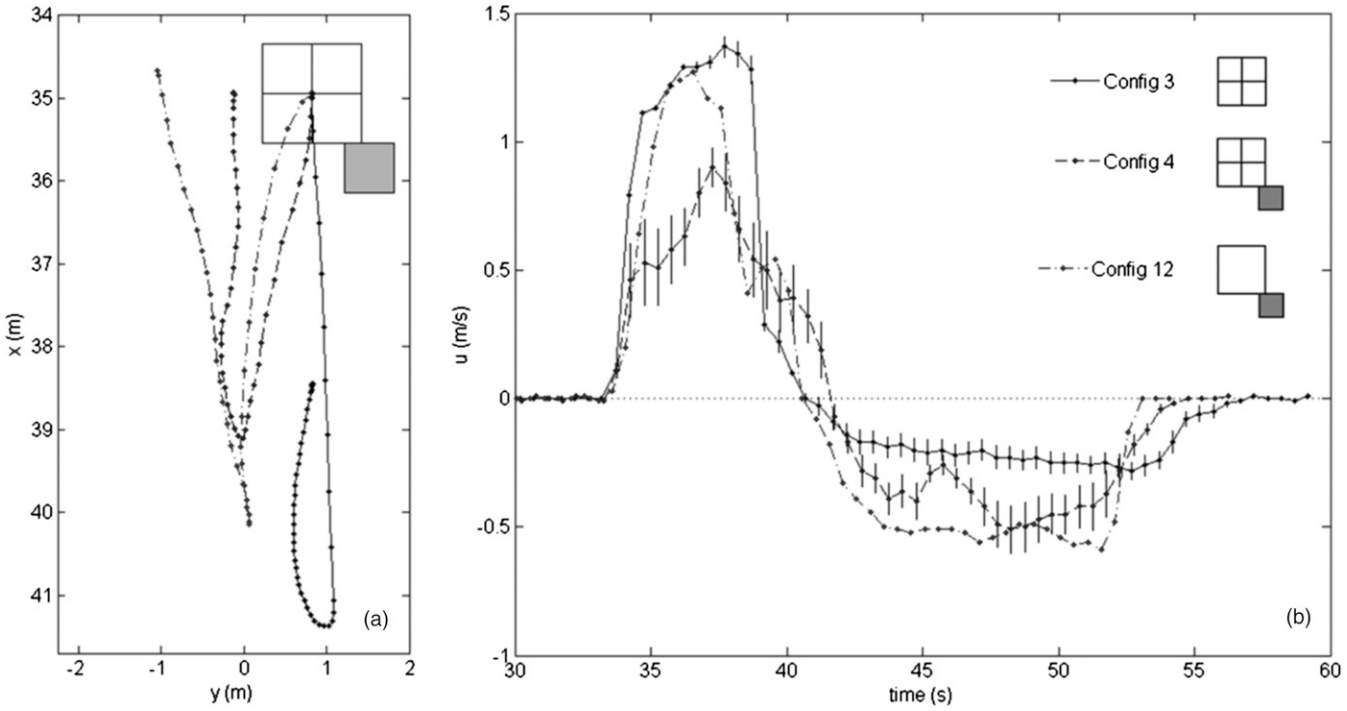

Fig. 17. Configurations 3, 4, and 12: only Trial 33 is used to represent Configuration 4; (a) path positions and (b) cross-shore (X-direction) velocities for multibox configurations (Configurations 3 and 4) are for the centroid, which is the arithmetic mean of all box centers for a single time step; positions and velocities for Configuration 12 are for the center of the four-box square; error bars for multibox configurations represent standard error of box velocities with 95% confidence intervals; schematic of initial box positions from Fig. 4 shown for Configuration 4 in plot (a) for reference and scale

Configurations 4 and 12, it can be observed that the peak of the four joined boxes is larger and occurs sooner than the four individual boxes. Review of Figs. 9(c and d) and 9(e and f) show the different nature of the initial motions of the boxes. The fact that Boxes 2 and 4 form a column that is hung up on the stationary box helps to explain the difference in the centroid velocities between Configurations 4 and 12. Despite these differences in initial velocity, the trajectories of the average centroid shown in Fig. 17(a) are surprisingly similar. Although the combined box reaches a more landward position, both centroids for the two configurations reach a final stopping point that is approximately the same cross-shore position at the starting point ($x = 35$ m).

Summary and Conclusion

This paper presents an analysis using optical techniques of tsunami-debris movement during laboratory experiments performed in a large-scale wave basin. Trials were run with up to nine mobile debris specimens on an elevated section fronted by an alongshore uniform slope. Specimens were placed in seven different initial configurations, some with an additional, fixed specimen to induce rotation. One initial configuration was tested six times to study the repeatability of the debris motion. Configurations were designed to study debris translation and rotation as well as the effects of debris quantity and segmentation of groups. Most of the data for this paper were collected by two overhead cameras, and optical tracking results from these cameras summarize both the wave and debris motion. In situ instruments such as ultrasonic wave gauges were used for timing and to estimate momentum flux in combination with the tracking results.

Based on this work, the following conclusions can be made:

1. Combining optical and in situ measurements for large-scale laboratory tsunami inundation studies can extend the temporal extent of the observations, and when combined with elevations measurements can be used to estimate the momentum flux, particularly during the leading edge of uprush (Fig. 6).
2. The optical debris tracking technique reliably tracks as many as nine boxes and can provide centroid position, velocity, angle, and rate of rotation (Fig. 9).
3. Centroid position and velocity of individual boxes and the average centroid position and corresponding velocity was highly repeatable during the onshore motion, including the position of the stall point. During the offshore motion, the centroid positions and velocities were more highly varied (Fig. 12). This variation was not because of measurement error; it may have been from the irregularities in the flow field.
4. For debris in free translation, as the number of debris specimens increased, the peak average velocity decreased and the onset of the peak was delayed in the onshore direction (Fig. 14). In the offshore direction, the velocity was lower by a factor 4–6 and was independent of the quantity of debris.
5. In contrast to the case of free translation, the forced rotation cases did not exhibit self-similar centroid paths or velocity time histories, owing to the complex nature of the initial motion [Fig. 15 and Figs. 9(b, f, and h)].
6. Peak onshore velocity is nearly independent of whether its initial motion is purely translational or a combination of rotation and translation (compare Configurations 1 and 2 in Fig. 16), and the size of the debris affects the peak onshore velocity for rotating debris (compare Configurations 2 and 12 for Fig. 16).

This laboratory investigation of idealized configurations shows that some aspects of the debris movement such as the onshore velocity or maximum landward extent of debris may benefit from deterministic modeling. However, the offshore motion including trajectories and final stopping points appears to be more varied and may benefit from probabilistic modeling, as suggested by one of the

paper's reviewers. Furthermore, future work should consider other parameters such as debris mass, phenomena such as debris-debris collisions, and realistic scenarios of actual debris shapes such as shipping containers, cars, or vessels, as was noted by one of the reviewers.

Acknowledgments

Support for this research by Oregon Sea Grant and the National Science Foundation under No. CMMI-0830378 is gratefully acknowledged. The Tsunami Facility is supported by the Network for Earthquake Engineering Simulation (NEES) Program of the National Science Foundation under award No. CMMI-0402490. The authors gratefully acknowledge the work of the staff of the O. H. Hinsdale Wave Research Laboratory and several other undergraduate student workers (Kyle Mayfield, Jose Lozano, and Brittany Snyder) in conducting the physical model experiments. The authors thank the two anonymous reviewers for their comments to improve the manuscript.

References

Arikawa, T., Ohtsubo, D., Nakano, F., Shimosako, K., and Ishikawa, N. (2009). "Large model tests of drifting container impact force due to surge front tsunami." *Proc., Conf. on Coastal Engineering*, Japan Society of Civil Engineers, Tokyo (in Japanese).

Arikawa, T., and Yashizaki, M. (2009). "Large scale tests on concrete wall destruction by tsunami with driftwood." *Proc., Conf. on Coastal Engineering*, Japan Society of Civil Engineers, Tokyo (in Japanese).

Baldock, T. E., Cox, D., Maddux, T., Killian, J., and Fayler, L. (2009). "Kinematics of breaking tsunami wavefronts: A data set from large scale laboratory experiments." *Coastal Eng.*, 56(5–6), 506–516.

Cox, D., Tomita, T., Lynett, P., and Holman, R. A. (2008). "Tsunami inundation with macro-roughness in the constructed environment." *Proc., 31st Int. Conf. on Coastal Engineering*, ASCE, Reston, VA, 1421–1432.

Foytong, P., Ruangrassamee, A., Shoji, G., Hiraki, Y., and Ezura, Y. (2013). "Analysis of tsunami flow velocities during the March 2011 Tohoku, Japan Tsunami." *Earthquake Spectra*, 29(S1), S161–S181.

Fritz, H. M., et al. (2012). "The 2011 Japan tsunami current velocity measurements from survivor videos at Kesennuma Bay using LiDAR." *Geophys. Res. Lett.*, 39(7), L00G23.

Goring, D. G. (1978). "Tsunamis—The propagation of long waves onto a shelf." *Rep. No. Kh-R-38*, W. M. Keck Laboratory of Hydraulics and Water Resources, California Institute of Technology, Pasadena, CA.

Gorst, N. J. S., Williamson, S. J., Pallett, P. F., and Clark, L. A. (2003). "Friction in temporary works." *Research Rep. 071*, Univ. of Birmingham, Birmingham, U.K.

Hayashi, S., and Koshimura, S. (2013). "The 2011 Tohoku Tsunami flow velocity estimation by the aerial video analysis and numerical modeling." *J. Disaster Res.*, 8(4), 561–572.

Holman, R. A., and Stanley, J. (2007). "The history and technical capabilities of Argus." *Coastal Eng.*, 54(6–7), 477–491.

MATLAB R2011b [Computer software]. Natick, MA, MathWorks.

Matsutomi, H. (2009). "Method for estimating collision force of driftwood accompanying tsunami inundation flow." *J. Disaster Res.*, 4(6), 435–440.

Mori, N., Takahashi, T., Yasuda, T., and Yanagisawa, H. (2011). "Survey of 2011 Tohoku earthquake tsunami inundation and run-up." *Geophys. Res. Lett.*, 38(7), L00G14.

Naito, C., Cercone, C., Riggs, H. R., and Cox, D. (2014). "Procedure for site assessment of the potential for tsunami debris impact." *J. Waterway, Port, Coastal, Ocean Eng.*, 10.1061/(ASCE)WW.1943-5460.0000222, 223–232.

Naito, C., Cox, D., Yu, Q.-S., and Brooker, H. (2013). "Fuel storage container performance during the 2011 Tohoku, Japan, tsunami." *J. Perform. Constr. Facil.*, 10.1061/(ASCE)CF.1943-5509.0000339, 373–380.

Okal, E. A., et al. (2010). "Field survey of the Samoa tsunami of 29 September 2009." *Seismol. Res. Lett.*, 81(4), 577–591.

Oshnack, M. B., Aguiniga, F., Cox, D., Gupta, R., and van de Lindt, J. (2009). "Effectiveness of small onshore seawalls in reducing forces induced by tsunami bore: Large scale experimental study." *J. Disaster Res.*, 4(6), 382–390.

Park, H., Cox, D. T., Lynett, P. J., Wiebe, D. M., and Shin, S. (2013). "Tsunami inundation modeling in constructed environments: A physical and numerical comparison of free-surface elevation, velocity, and momentum flux." *Coastal Eng.*, 79(Sep), 9–21.

Park, S., van de Lindt, J. W., Cox, D., Gupta, R., and Aguiniga, F. (2012). "Successive earthquake-tsunami analysis to develop collapse fragilities." *J. Earthquake Eng.*, 16(6), 851–863.

Reuben, M., Holman, R., Cox, D., Shin, S., Killian, J., and Stanley, J. (2011). "Optical measurements of tsunami inundation through an urban waterfront modeled in a large-scale laboratory basin." *Coastal Eng.*, 58(3), 229–238.

Ruangrassamee, A., Yanagisawa, H., Foytong, P., Lukkunaprasit, P., Koshimura, S., and Imamura, F. (2006). "Investigation of tsunami-induced damage and fragility of buildings in Thailand after the December 2004 Indian Ocean tsunami." *Earthquake Spectra*, 22(S3), S377–S401.

Saatcioglu, M., Ghobarah, A., and Nistor, I. (2006). "Performance of structures in Thailand during the December 2004 Great Sumatra earthquake and Indian Ocean tsunami." *Earthquake Spectra*, 22(S3), S355–S375.

Takahashi, S., et al. (2010). "Joint survey for 2010 Chilean earthquake and tsunami disaster in ports and coasts." *PARI Technical Note 1224*, Port and Airport Research Institute, Kuriyama, Japan.

Thomas, S., and Cox, D. (2012). "Influence of finite-length seawalls for tsunami loading on coastal structures." *J. Waterway, Port, Coastal, Ocean Eng.*, 10.1061/(ASCE)WW.1943-5460.0000125, 203–214.

USGS Tsunami Pilot Study Working Group. (2006). "Seaside, Oregon tsunami pilot study—Modernization of FEMA flood hazard maps." *Open-File Rep. 2006-1234*, U.S. Dept. of the Interior, USGS, Washington, DC.

Yeom, G., Nakamura, T., and Mizutani, N. (2009). "Collision analysis of container drifted by run-up tsunami using drift collision model." *J. Disaster Res.*, 4(6), 441–449.